Earth Planet. Sci. Lett. 695 (2026) 120349

Contents lists available at ScienceDirect

Earth and Planetary Science Letters

journal homepage: www.elsevier.com/locate/epsl

Geological characterization of Shackleton-Slater crater region at lunar south pole, Chang'e-7 candidate landing site

Mingyu Tian [a], Yuqi Qian [a,*], Lukas Wueller [b,c], James Head [c], Xiang Li [d], Wajiha Iqbal [b,c], Harald Hiesinger [b], Carolyn van der Bogert [b], Ke Xu [e], Lingzhi Sun [f], Long Xiao [g], Guochun Zhao [a,h,**]

[a] NWU-HKU Joint Center of Earth and Planetary Sciences, Department of Earth and Planetary Sciences, The University of Hong Kong, Hong Kong, China
[b] Institut für Planetologie, Universität Münster, Münster, Germany
[c] Department of Earth, Environmental and Planetary Sciences, Brown University, Providence, USA
[d] Anhui Institute of Optics Fine Mechanics, Chinese Academy of Sciences, Hefei, China
[e] Department of Energy and Resources Engineering, College of Engineering, Peking University, Beijing, China
[f] Hawai'i Institute of Geophysics and Planetology, University of Hawai'i at Mānoa, Honolulu, USA
[g] School of Earth and Planetary Sciences, China University of Geosciences, Wuhan, China
[h] NWU-HKU Joint Centre of Earth and Planetary Sciences, State Key Laboratory of Continental Evolution and Early Life, Department of Geology, Northwest University, Xi'an, China

ARTICLE INFO

Editor: Dr O Mousis

Keywords:
Lunar south pole
Lunar water ice
South Pole-Atiken basin
Chang'e-7

ABSTRACT

The lunar south pole is a priority target for modern robotic and human lunar explorations. The high significance of the region for scientific research and resource utilization stems from the potential presence of volatiles. The upcoming Chang'e-7 mission, scheduled for 2027, will conduct comprehensive in situ explorations of this region. The Chang'e-7 candidate landing site is located between Shackleton and Slater craters. In this study, we conducted a comprehensive analysis of the Chang'e-7 candidate region. Multi-source remote sensing data were used to characterize the regional topography, geomorphology, and chemical composition, and to perform impact modeling to trace the provenance of landing site materials. Our results reveal that the landing site is dominated by anorthositic materials with low-Ca pyroxene signatures. Impact ejecta thickness calculation indicates the landing region is primarily composed of materials from the Imbrian-aged Shackleton crater (~11.6 m of primary ejecta), with significant contributions from impact basins within the South Pole-Aitken basin, such as Amundsen-Ganswindt and Schrödinger, which were redistributed and buried by Shackleton ejecta. Water ice reflectance features indicated potential surface and subsurface ice at the nearby permanently shadowed region of Crater S (unofficial name). This suggests that it is necessary to explore this region with newly developed payloads and extract subsurface regolith for volatile measurements. This study provides a critical geological framework for the Chang'e-7 mission, offers testable hypotheses for its scientific operations, and contributes to a broader understanding of lunar polar geology, volatile distribution, and the evolution of the South Pole-Aitken basin.

1. Introduction

The lunar south pole has long been a focal point of lunar exploration, with the potential presence of volatile resources and materials recording the Moon's early evolution (Flahaut et al., 2020). Because of the extremely low surface temperatures in permanently shadowed regions (PSRs) near the poles, more water ice might be possessed there than in mid- and low-latitude regions (Li et al., 2018). The south polar region has a more continuous distribution of PSRs (Fig. 1A), thus becoming a priority target for modern robotic and human lunar explorations. Located at the southern edge of the South Pole-Aitken (SPA) basin, the Shackleton crater region is an ideal place to study lunar volatiles and the lunar interior structure. The SPA impact event is the last major impact event that reshaped the immediate south polar region, offering access to

* Corresponding author.
** Corresponding author at: NWU-HKU Joint Centre of Earth and Planetary Sciences, State Key Laboratory of Continental Evolution and Early Life, Department of Geology, Northwest University, Xi'an, China.
E-mail addresses: yuqiqian@hku.hk (Y. Qian), gzhao@hku.hk (G. Zhao).

https://doi.org/10.1016/j.epsl.2026.120349
Received 12 May 2026; Received in revised form 8 September 2026; Accepted 10 September 2026
Available online 18 September 2026
0012-821X/

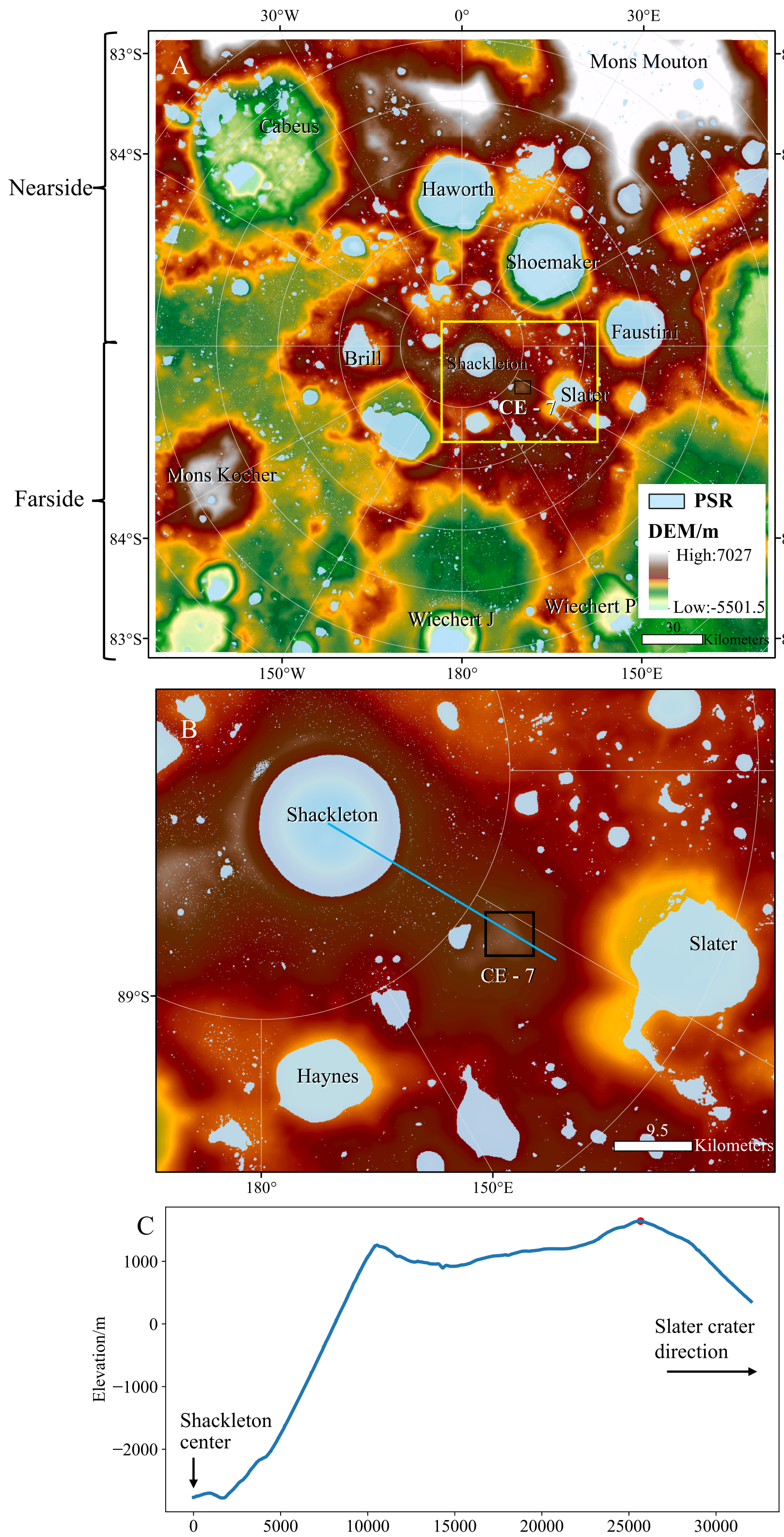

Fig. 1. The CE-7 candidate landing region. (A) DEM of 85° S to the south pole, the light blue polygons represent PSRs. (B) Zoom in view of the yellow square region in (A). (C) The vertical exaggerated DEM profile (Barker et al., 2023) of the blue line in (B), the red dot represents the CE-7 candidate site.

materials with clear provenance from surface to subsurface (Wueller et al., 2026c).

Previous studies showed that lunar interior materials from deep crust, even upper mantle, might be excavated and dispersed across SPA (Melosh et al., 2017; Moriarty et al., 2021). This distribution extends to the south pole, especially if the impact was southward (Andrews-Hanna et al., 2025), with significant implications for this giant impact. However, only two missions have landed within SPA so far: the Chang'e-4 (CE-4) and Chang'e-6 missions (CE-6). Neither did these missions provide conclusive evidence of SPA materials as they landed on mare regions. A south pole mission is able to offer solid evidence of the SPA basin materials with its high concentration in the region (Frueh et al., 2025; Moriarty and Pieters, 2018; Wueller et al., 2025).

Several upcoming missions (e.g., Artemis 4, Chang'e 7/8, Chandrayaan-4, Luna 27) are targeting the lunar south pole for studying key scientific questions related to volatiles and the SPA formation. The Chang'e-7 (CE-7) mission of the Chinese Lunar Exploration Program will present unprecedented capabilities to address them, consisting of a communication relay satellite, an orbiter, a lander, a rover, and a hopper (Wang et al., 2024). The CE-7 mission is scheduled to launch in 2027. The region between Shackleton and Slater craters (hereinafter Shackleton-Slater Ridge) is the priority landing site (88.8°S, 123.4°E) (Fig. 1B). It offers solar illumination (>60% of the year) (Mazarico et al., 2011), Earth visibility (Mazarico et al., 2011), and surface slopes less than 5 degrees (Barker et al., 2023), enabling a safe landing. The main scientific goal of CE-7 is to search for water and SPA materials. CE-7 will carry a Lunar Neutron Gamma Spectrometer and a Wide-band Infrared Spectrum Mineral Imaging Analyzer (WISMIA) onboard the orbiter, an In situ Measuring System of Volatiles (IsMSV), a Lunar Raman Spectrometer (LRS), a Lunar Penetrating Radar (LPR) onboard the rover, and a Lunar Soil Water Molecular Analyzer (LSWMA) onboard the hopper that will explore PSRs (Wang et al., 2024). LSWMA will measure the isotopes of volatiles (hydrogen and oxygen) within PSRs to determine the source of lunar water; IsMSV will conduct in situ measurements of water content and variation with unprecedented accuracy (0.01 wt.%) to determine the distribution and abundance of lunar water (Li et al., 2025; Wang et al., 2024). These would greatly help to study the distribution and composition of SPA-derived materials and potential volatile resources.

Therefore, a comprehensive, pre-landing study of the CE-7 candidate region is essential to inform and guide surface operations and in situ exploration. We first characterized the topographic, geomorphologic, and geological setting of the CE-7 candidate region (Sections 3.1 and 4.1), identifying the surrounding geomorphic features that may influence landing safety and scientific access. Secondly, we modeled the provenance and stratigraphy of the landing site materials through impact ejecta thickness calculations (Sections 3.2 and 4.2) (Neumann et al., 2015; Sharpton, 2014; Wang et al., 2021; Xu et al., 2021). This directly addressed which materials CE-7 will likely investigate. Then, we analyzed the surface chemical and mineralogical composition of the candidate site (Lemelin et al., 2022) (Sections 3.3 and 4.3). This compositional characterization defines the lithology that CE-7 will likely encounter *in situ*. It also provides a compositional fingerprint for tracing the provenance of materials delivered to the landing site from distant craters and basins. Lastly, we used multiple datasets to study potential surface water/ice and subsurface ice.

Our study addresses two main questions: (1) What impact sources contributed to the regolith, and how are their ejecta distributed stratigraphically? (2) What geological context does the landing site provide for future investigations of lunar volatiles?

2. Data and methods

2.1. Topography and geomorphology

Lunar Reconnaissance Orbiter (LRO) Wide-Angle Camera (WAC, spatial resolution 100 m/pixel) (Wagner et al., 2015) and Lunar Orbiter Laser Altimeter Digital Elevation Model (LOLA DEM) were used to analyze the topography and geomorphology of the lunar south pole. The Narrow Angle Camera (NAC, spatial resolution 1 m/pixel) (Archinal et al., 2023) polar region mosaic was also used for studying small-scale topographical structures. For LOLA DEM, the spatial resolution is 10 m/pixel southward of 85 °S, and 5 m/pixel southward of 87.5°S. These data are accessible from LOLA PDS Data Node (https://imbrium.mit.edu/DATA/LOLA_GDR/POLAR/FLOAT_IMG/) and the LROC website (https://pds.lroc.im-ldi.com/data/LRO-L-LROC-5-RDR-V1.0/LROLRC_2001/DATA/BDR/NAC_POLE/NAC_POLE_SOUTH/).

Two geological maps were used. The geological map of Krasilnikov et al. (2023) was used as a major reference for the south polar region. This map covers a range from 70°S to 90°S at a scale of 1:300,000. Five major types of geological units and structures were mapped, including high-standing SPA massifs, basins and crater materials, plains-forming units, crater wall terraces/wall-floor arcuate lobes, and lobate scarps. The global 1:5,000,000 scale geological map (Fortezzo et al., 2020) was used for global stratigraphic context. The mapped geological units include materials of craters, basins, terra, plains, Imbrium Formation, Orientale Formation, and volcanic units. In addition, the SPA geological map (Iqbal et al., 2026) and the high-resolution map (Wueller et al., 2026c) could complement the previous two maps at different scales. This would allow local observations to be correlated and linked to regional or global geological units, and vice versa.

2.2. Ejecta thickness calculation

We applied the ejecta thickness model of Sharpton (2014) to calculate the ejecta thickness at the CE-7 candidate site, as it was tested for lunar impact craters. For a given crater with radius R and center point located at a spherical distance r from the CE-7 candidate site, the primary ejecta thickness T (in m) for simple (smaller) craters and complex (larger) craters was calculated by:

$$T = \begin{cases} 0.014R^{1.01}(r/R)^{-3}, & 250m < R < 8.5km \\ 3.95(\pm 1.19)R^{0.399}(r/R)^{-3}, & 8.5km < R < 100km \end{cases} \quad (1)$$

Because all impact basins pre-date the formation of Shackleton crater between 3.43-3.69 Ga (Kring et al., 2021; Tye et al., 2015; Spudis et al. 2008), therefore, any basin ejecta materials near the south pole were overlain by Shackleton ejecta. However, subsequent impact gardening might have re-excavated basin ejecta to the surface. Therefore, we used Pike's model to calculate the basin ejecta thickness (in meters):

$$T = 0.033R_t(r/R_t)^{-3.0} \quad (2)$$

Where R_t is the transient rim-to-rim radius (half of the transient rim-to-rim distance) of the basin. As the radius of all basins are larger than the simple to complex transitional radius $R_{SC} = 9.5km$, we used $R_t = 0.5R$ (Croft, 1985), where R is the final rim-to-rim radius. The coordinates and radius data of basins are based on Neumann et al. (2015). For Orientale, Schrödinger, and Imbrium basins, their transient radii were referred to Xie and Zhu (2016), Xu and Xie (2020), Miljković et al. (2013), respectively.

In addition, distance corrections and deposition corrections were conducted for craters >1,500 km away from the candidate landing site (Xu et al., 2021). In the distance correction step, the revised distance d (R_S) is calculated by:

$$d(R_S) = R_{at} + \frac{2R_m tanX}{tanX + 1} \quad (3)$$

Where R_m is the average radius of the Moon (1,737.1 km). R_{at} is the transient radius at the lunar surface, which equals to approximately 0.5R (Croft, 1985) for basins. For simple craters, R_t is considered as 0.84R, and for complex craters, R_t would be calculated as $R_{SC}^{0.15}R^{0.85}$, where R_{SC} = 9.5 km is the transition radius. X equals to $R_S/(2R_m)$, $R_S = r - R_{at}$, and $R_{at} = 0.83R_t$ for craters.

As for the deposition correction, for a selected square of interest (SOI), the length of the SOI is considered as $L_{SOI} = \frac{1}{4}R_{at}$. Then an inner boundary and an outer boundary could be defined as $r_{inner} = d(r - L_{SOI}/2)$ and $r_{outer} = d(r + L_{SOI}/2)$, respectively. The geometrical mean distance $\bar{r}$ is calculated by $\bar{r} = \sqrt{r_{inner}r_{outer}}$. Considering the actual area on a spherical planetary body, the average primary ejecta thickness within the SOI could be calculated as $T_{SOI} = \frac{S_{ringflat}}{S_{ring}}T(\bar{r})$ (Xu et al., 2021) where

$$S_{ring} = 2\pi R_m^2 \left(\cos\left(\left(d_{sphere} - L_{SOI}\right) / 2\right) / R_m\right) - \cos\left(\left(d_{sphere} + L_{SOI}\right) / 2\right) / R_m\right)) \tag{4}$$

$$S_{ring\_flat} = \pi\left(r_{outer}^2 - r_{inner}^2\right) \tag{5}$$

In this study, uncertainties in ejecta thickness calculations were assessed using a Monte Carlo bootstrap approach with 500 iterations. In each iteration, the coefficients of the (Sharpton, 2014) scaling law were randomly sampled from normal distributions based on their reported uncertainties ($\pm$0.004 for simple craters and $\pm$1.19 for complex craters) (Sharpton, 2014; equation (5) and (6)), crater radii were perturbed by $\pm$5%, and the landing site coordinates by $\pm$180 m. The 2.5th and 97.5th percentiles of the resulting thickness distributions define the 95% confidence intervals (in m) reported in Table 1 and S1.

The primary ejecta would mix with local materials. The mixing model is used to calculate the mixing ratio μ' of local materials with ejecta materials.

$$\mu' \begin{cases} \mu, & \mu \leq 5 \\ \mu/2 + 2.5, & \mu \geq 5 \end{cases} \tag{6}$$

where $\mu = 0.0183r^{0.87}$(km) (Oberbeck et al., 1975).

The crater database LU1319373 from (Wang et al., 2021) was used for computing their foreign ejecta thicknesses at the CE-7 candidate site. In this dataset, craters >1–2 km (diameter) were extracted nearly completely from global DEM data using a machine-learning-based method. This dataset contains a total of approximately 1.32 million craters. For each crater, the recorded information includes: the longitude and latitude coordinates of the crater center, crater diameter, crater depth, the slope of the crater wall, the height of the crater rim, and the width of the crater floor. The coordinates and diameter were used in our calculations.

2.3. Chemical composition

The spectral products from Lemelin et al. (2022) were used for middle and high-latitude regions. This dataset was produced based on Kaguya Spectral Profiler (SP) data, using its spectra between 512.6 and 1,571.7 nm and calibrated to the LOLA reflectance at 1,064 nm. The dataset includes FeO, low calcium pyroxene (LCP), high calcium pyroxene (HCP), olivine (OLV), and plagioclase (PLG) contents from 50°S to 90°S with a spatial resolution of 1 km/pixel and an uncertainty of ~9 wt.% (Lemelin et al., 2022). Qiu et al. (2025) used the spectral data of Clementine Ultraviolet/Visible (UVVIS) and a linear relationship between oxide content and spectral reflectance to derive TiO_2 contents (100/200 m/pixel resolution for Ultraviolet/Visible, 1.17 wt.% uncertainty). The TiO_2 content was also used in this study.

We also used SP data to extract the spectral characteristics of the landing site. Kaguya SP acquired reflectance spectra between 500 and 2,600 nm (Visible Band, 0.5-1 μm; Near Infrared Band 0.9-1.7 μm; Near Infrared Band 2, 1.7-2.6 μm) with a ~500 m footprint (Haruyama et al., 2008; Yamamoto et al., 2014). Klima et al. (2007) calculated two main absorption band centers (Band I at 1,000 nm, Band II at 2,000 nm) of typical lunar silicate minerals, including Mg-OPX, Fe-OPX, LCP, HCP, and Wo50 pyroxene, which were used to identify the major mineral type at the CE-7 candidate region.

2.4. Volatile-related datasets

The Moon Mineralogy Mapper (M^3) (Green et al., 2011) global mode data (spatial resolution 140 m/pixel) were used. M^3 provides wider spectral coverage than SP with a wavelength range of 460-3,000 nm, covering absorption features of water species (i.e., OH^-, water ice, H_2O) at 1,300, 1,

Table 1
The list of 10 major craters and 6 basins that contribute the most foreign materials.

Name	Longitude	Latitude	Radius/M	Ejecta thickness/M	Local material thickness/M	Thickness/M	Age/GA
SHACKLETON	131.07	-89.65	10671.60	11.6 (95% CI: 4.1-24.0)	3.6	15.2	3.51[a]
WIECHERT J	-177.67	-85.24	17568.50	0.5 (95% CI: 0.2-1.0)	0.6	1.1	3.2[b]
ANTONIADI	-172.99	-69.60	68255.00	0.5 (95% CI: 0.2-1.0)	2.3	2.8	3.2-3.7[c];
HAUSEN	-88.57	-65.39	81679.95	0.4 (95% CI: 0.2-0.9)	2.3	2.7	~3[d]
	97.76	-88.94	2696.05	0.2 (95% CI: 0.1-0.5)	0.0	0.2	
NUMEROV	-162.23	-70.57	50881.05	0.2 (95% CI: 0.2-1.0)	0.9	1.1	
HALE	91.79	-74.23	40370.20	0.2 (95% CI: 0.1-0.4)	0.7	0.9	Upper Imbrian-aged[e]
	-138.15	-83.71	18496.65	0.2 (95% CI: 0.06-0.3)	0.3	0.5	
	134.24	-88.61	1728.05	0.2 (95% CI: 0.05-0.4)	0.0	0.2	
	-94.55	-88.34	8488.25	0.1 (95% CI: 0.04-0.4)	0.1	0.2	
	151.71	-88.70	2790.45	0.1 (95% CI: 0.04-0.4)	0.0	0.1	
BASINS							
AMUNDSEN-GANSWINDT	123	-81	189000	263	559	822	4.26[f]
Schrödinger	133.5	-74.9	163000	35	124	159	3.86[f]
AUSTRALE NORTH	96	-35.5	440000	17	138	155	
ORIENTALE	-94.8	-20.1	468500	16	153	169	3.81[f]
MENDEL-RYDBERG	-94.6	-49.8	325000	12	83	95	4.13[f]
IMBRIUM	-18.5	37	660500	8	109	117	3.87[f]

Age references:
[a] . (Tye et al., 2015);
[b] .(Deutsch et al., 2020)
[c] . (Sruthi and Senthil Kumar, 2014);
[d] . (Hawke et al., 2004);
[e] . (Iqbal et al., 2026);
[f] . (Orgel et al., 2018). Note that Australe North is just a proposed basin (Neumann et al., 2015) and not yet proven.

500, 2,000, and 2,850 nm (Li et al., 2018; Pieters et al., 2009). The Level 2 reflectance data acquired during the OP2C optical period have undergone thermal and photometric corrections, with uncertainty <10% (Green et al., 2011). However, the signal levels of the M^3 data are limited for high-latitude regions due to poor illumination conditions. Therefore, we used LOLA 1064 nm reflectance (spatial resolution 1 km/pixel) to help characterize water/ice signals within PSRs. These data are the reflectance of the surface measured at zero phase angle relative to a Lambert surface illuminated at the same geometry, and are in units of normal albedo (Fisher et al., 2017) (http://pds-geosciences.wustl.edu/lro/lro-l-lola-3-rdr-v1/lrolol_1xxx/data/). The off/on ratio data (off-band: 155.57–189.57 nm, on-band: 129.57–155.57 nm) of the Lyman Alpha Mapping Project (LAMP) was also used for searching water/ice signals (Gladstone et al., 2012; Hayne et al., 2015), as it has higher SNR in polar regions than M^3.

Two datasets were also used to analyze the potential existence of subsurface water ice, including ice stability depth (ISD, ~200 m/pixel) (Siegler et al., 2016) and ice favorability index (IFI, ~532 m/pixel) (Cannon and Britt, 2020). The ice stability depth is determined by an updated thermal model of (Siegler et al., 2016). Three types of ice sources were considered to derive the IFI, namely the carbonaceous asteroids and comets, volcanic outgassing from the lunar interior, and solar/Earth wind implantation (Cannon and Britt, 2020). The IFI was then calculated by modeling the ice capture and ice retention process.

3. Results

3.1. Local topography and geomorphology

The CE-7 candidate landing region is located ~25.7 km away from the center of Shackleton crater (Fig. 1A, 1B), at Shackleton-Slater Ridge. The candidate site is located on a local topographic peak with an elevation of ~1,600 m, surrounded by slopes steeper than 10° (Fig. 1C). Compared to the surrounding region, the selected site is about 400 m higher. The candidate landing site has an average yearly solar illumination of ~60% (Mazarico et al., 2011). Boulders are abundant along the rim of Shackleton crater and several smaller craters around the landing site (Boazman et al., 2022) (Fig. S1).

Most craters in the 85-90°S study region are distributed on the nearside, with diameters up to ~50 km. The largest three craters (Haworth, Shoemaker, and Faustini) are highly degraded and have relatively smooth rims. Secondary craters are widely distributed within the entire study region, with irregular morphology, spatial occurrences in chains and/or clusters that exhibit herringbone-shaped morphology.

Light plains with very shallow slopes (less than 2°) exist in the floor of a few large craters (e.g., Shoemaker, Faustini, Sverdrup) (Qiao et al., 2024) (Fig. S1). Because of the mapping scale, some smaller light plains that occur in small, isolated patches were mapped in our new study (Wueller et al., 2026c).

As the study region is close to the SPA rim, a few topographically prominent massifs appear near the edge of the study region (e.g. Mons Kocher, Mons Malapert). These Mons are several kilometers higher than their surrounding regions, about 50-100 km in width. All of them are interpreted as remnant rims of the SPA basin (Bernhardt et al., 2025; Wueller et al., 2025, 2024).

The geological units within the study region range from Pre-Nectarian to Copernican in age (Fig. 2). The underlying layer of this region is the undivided Pre-Nectarian basin materials (the SPA basin is the basis here), and is covered by primary and secondary craters. Mons Kocher, Mons Cabeus, Mons Malapert, and Mons Mouton surrounded half of the study region near 85°S. The ridge that Shackleton crater is located on could also be interpreted as a remnant rim massif of the SPA basin (Frueh et al., 2025; Gawronska and Boazman, 2025).

Pre-Nectarian-aged craters are the dominant craters. This includes Haworth, Shoemaker, Faustini, etc. (Fig. 2). Most Pre-Nectarian and Nectarian-aged craters have light plains on their crater floors (Qiao et al., 2024; Wueller et al., 2026c). Several Imbrian-aged craters are distributed within the study region, including Kocher, Wiechert J, etc. The Shackleton crater is characterized as an Imbrian-aged crater (Krasilnikov et al., 2023; Wueller et al., 2026c). The diameters of the four Eratosthenian craters are all less than 12 km, but the range of their ejecta blankets could extend to larger than three times the crater diameter (Krasilnikov et al., 2023).

3.2. Provenance of materials

Based on the Sharpton (2014) ejecta thickness model, 163 craters that contribute a primary ejecta thickness thicker than 5 cm were identified. As the CE-7 candidate site is primarily located within the ejecta of Imbrian-aged Shackleton crater (about 2.6 times Shackleton's radius, see also discussion) (Krasilnikov et al., 2023), 121 craters of Nectarian and Pre-Nectarian ages were excluded based on the two geological maps mentioned above. The distribution of the 42 major source craters (Fig. 3) is relatively homogeneous from all directions. Among these 42 craters, 29 of them are within the SPA basin, and brought ~22.8 m of foreign material to the landing site. Other craters did not bring large amounts of foreign ejecta as Shackleton did, but the local material was excavated and mixed lots of times by impact gardening.

To further constrain the number of source craters, we comprehensively investigated the morphology of all 42 craters. Craters that are degraded or were reported to be older than Shackleton at 3.43-3.69 Ga (Kring et al., 2021; Tye et al., 2015; Spudis et al. 2008) were excluded. The degraded craters include 24 craters that have no obvious crater rim, and craters that possess a lot of secondary craters or light plains (Fig. S2). Eight small source craters whose ejecta blankets are hard to identify, typically with a radius < 2 km, were treated as young craters. Two secondary craters were identified as Imbrian-aged (Krasilnikov et al., 2023).

Within the remaining 18 source craters, the crater that contributed the highest amount of ejecta is the Shackleton crater. It brought ~11.6 m of foreign ejecta material to the CE-7 candidate site, ~15.2 m in total (with the mixed local material, ~60% of the total ejecta thickness). The true thickness of emplaced Shackleton ejecta may be higher, and that mixing may be less intense based on the topography of the landing site with respect to Shackleton crater (Wueller et al., 2026c). Followed by Wiechert J and Antoniadi craters that could contribute ~0.5 m of ejecta materials. The total thickness of ejecta brought by Imbrian-aged craters was ~13 m. Compared to this, the Eratosthenian-aged craters (e.g., Hausen) contribute a small amount of foreign ejecta.

The bootstrap-derived 95% confidence intervals for the primary ejecta thicknesses are listed in Table 1. For Shackleton crater, the nominal thickness of ~11.6 m corresponds to a 95% confidence interval (CI) of 5.8–18.1 m, reflecting the propagation of uncertainties in the Sharpton model coefficients through the non-linear power-law scaling.

As the radius of basins is much larger than most of the craters, around 26 basins contributed foreign ejecta thicker than 1 m. Here, we selected 6 basins that contribute the most foreign ejecta (thicker than 7 m) for further analyses. These basins include Amundsen-Ganswindt, Schrödinger, Orientale, Australe North, Mendel-Rydberg, and Imbrium. Detailed ejecta thickness values are listed in Table 1 (Table S1 for full list).

3.3. Surface chemical composition and implications for ejecta provenance

Fig. 4 shows the compositional characteristics of the CE-7 candidate landing region (Lemelin et al., 2022). The FeO content of the landing

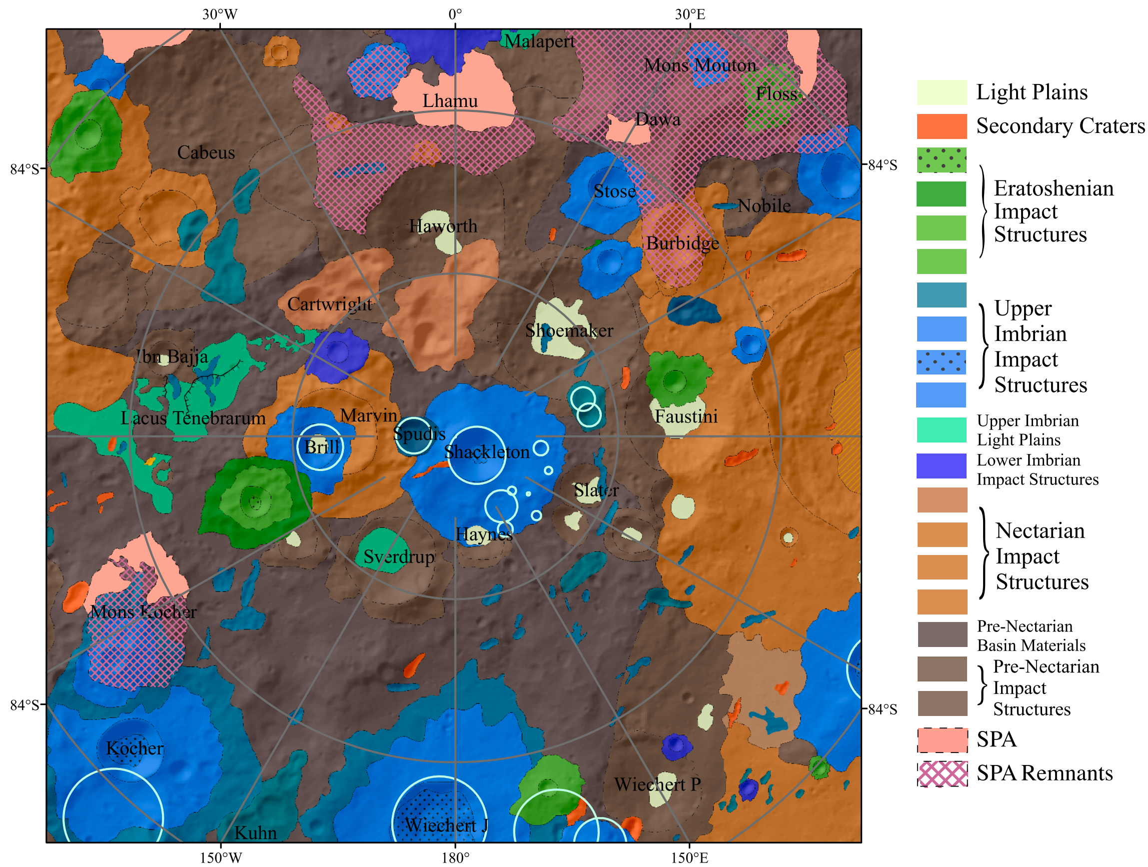

Fig. 2. Geological map (Krasilnikov et al., 2023) of the study region and correlation of map units. The blue circles are craters that contribute >5 cm foreign ejecta to the CE-7 candidate site and are potentially younger than Shackleton crater. The age of these craters will be determined later by their morphology.

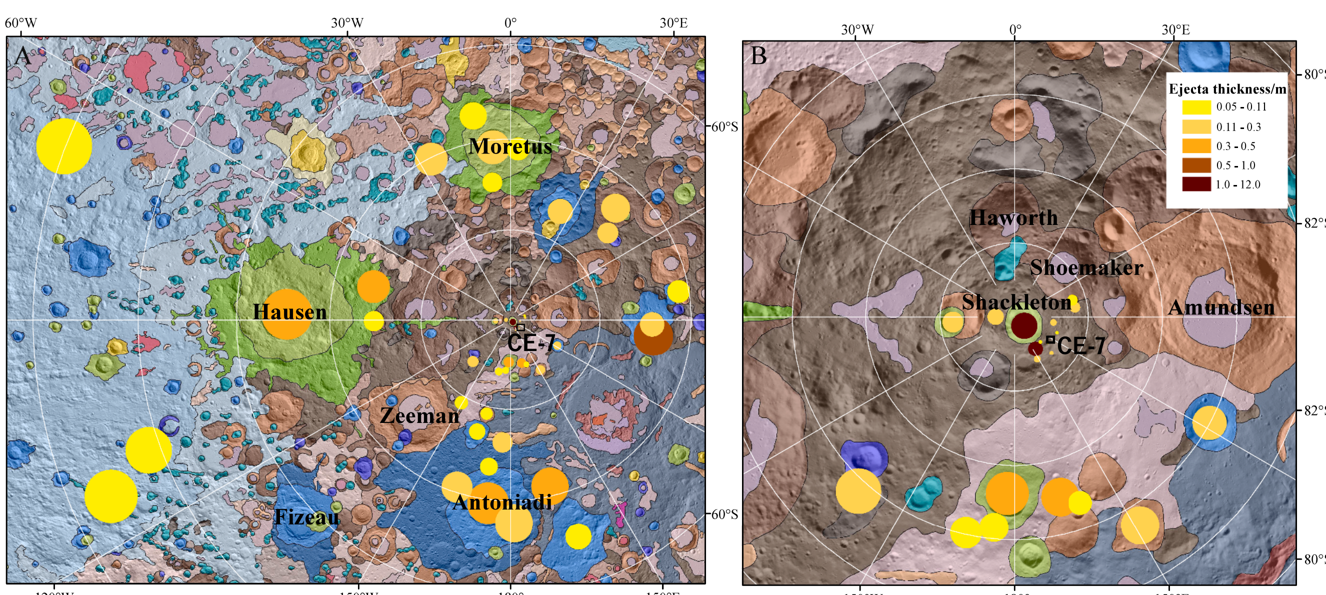

Fig. 3. (A) The distribution of source craters and the ejecta thickness they contributed. (B) The zoom in view near the south pole of (A). The background image is LOLA hillshade and USGS geological map.

region varies between 5% and 8%. However, the ejecta deposits of Shackleton and Faustini craters show lower FeO contents than surrounding regions, suggesting an anorthositic composition, potentially crustal materials from an uplifted SPA basin rim (Frueh et al., 2025; Moriarty and Petro, 2024; Wueller et al., 2026c). Although the TiO_2 content data only partly covers the study region, it still indicates that the TiO_2 content is low

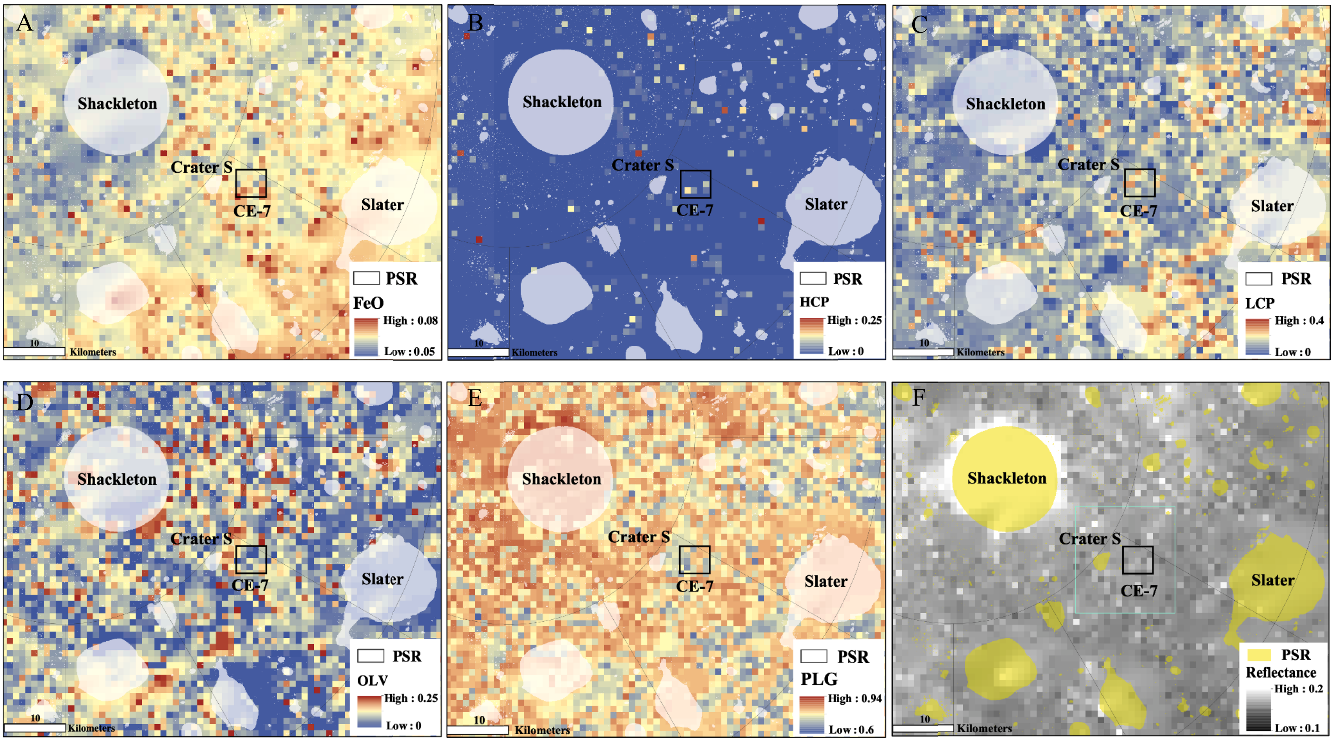

Fig. 4. Surface chemical composition of CE-7 candidate region. (A) Kaguya SP FeO abundance, (B) Kaguya SP HCP abundance, (C) Kaguya SP LCP abundance, (D) Kaguya SP OLV abundance, (E) Kaguya SP PLG abundance, and (F) The reflectance of Kaguya SP at 800 nm. The red stars and black frames represent the CE-7 candidate site, the white/yellow regions represent PSRs.

(<1%) near the south pole (southern than 87.5°S), while the content can reach up to 17% near (-87°S, 150°W), probably indicating a cryptomare region.

As for the mineralogical contents, the HCP contents inside the study region are almost all below the detection limit. PLG is the dominant mineral phase (~76±6%) at the CE-7 candidate landing site. The content of LCP becomes lower (~10%) toward the south pole than in regions north of ~87°S (~20%). At the CE-7 candidate site, the OLV content is about 5.4 ±4%. We analyzed the lithology (Fig. 5A) of CE-7 candidate site based on the scheme of Stöffler et al. (1980). It contains ~81% PLG and ~7% LCP; HCP was not detected, which could be classified as anorthosite. Chemical compositions of 85°S to the lunar south pole are shown in Fig. S3.

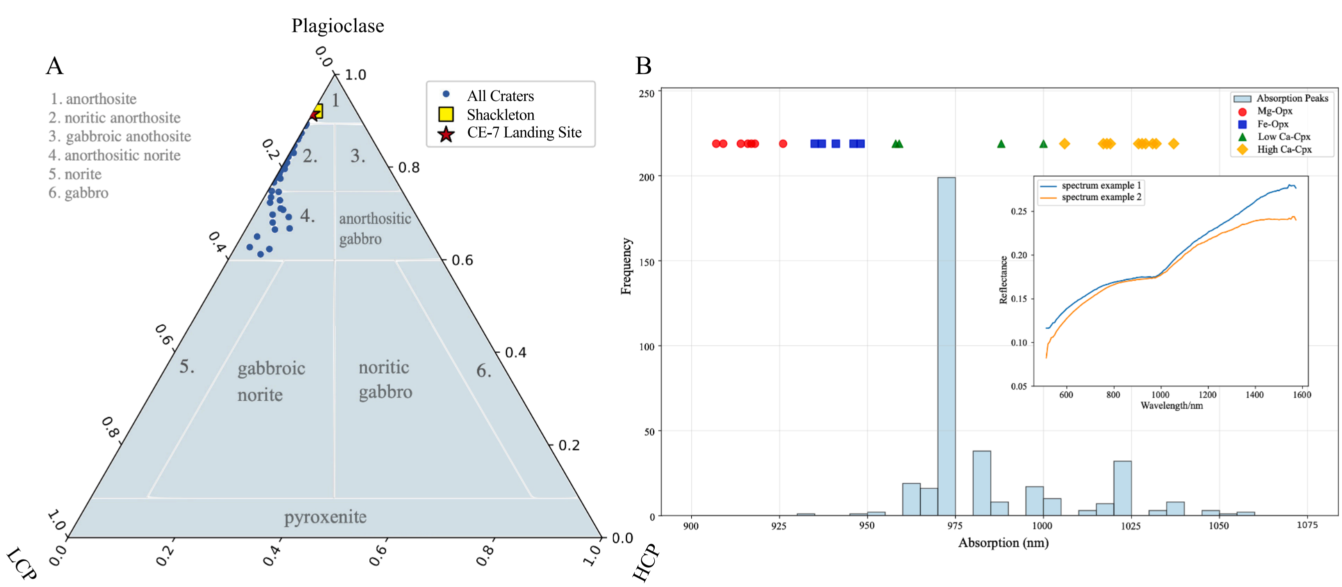

Fig. 5. (A) Lithology of CE-7 candidate site and 42 source craters that contribute larger than 5 cm foreign ejecta. (B) Band I absorption features of 323 spectra at the landing site, also showing two spectra at the CE-7 candidate site as examples.

The spectral absorption features in the region near the CE-7 candidate site (Fig. 5B) were analyzed. Spectra of 323 pixels of the topographic peak at the CE-7 candidate landing site were extracted, and the absorption centers of each spectrum were calculated. The histogram of the absorption center was plotted and compared to the dataset of Klima et al. (2007). Due to the limited wavelength range of the spectral data (512-1,571 nm), only the Band I center was used. The statistical result showed that the absorption center concentrated near 975 nm, matching the absorptions of LCP, indicating that the CE-7 candidate region mainly consists of LCP, consistent with Kaguya's mineralogical datasets.

For the remaining 42 craters (Fig. 3), the average HCP, LCP, and PLG contents within the crater rims were extracted, with at least tens of pixels in area (Fig. 5A). The surface chemical composition of Shackleton crater and the CE-7 candidate site are the most similar, which is consistent with the interpretation that Shackleton is the predominant source of local ejecta. The HCP contents of all source craters are low, with half of them less than 2%, and the highest under 8%, all within the errors of the data. Meanwhile, the PLG contents remain higher than 90%.

3.4. Volatile characteristics

M^3 spectrum of the CE-7 candidate site shows an absorption feature near ~2,850 nm (Fig. 6A, B), which might be hydroxyl signals (Li and Milliken, 2017). LOLA reflectance data showed an average albedo of 0.37±0.01 at the CE-7 candidate landing site, and 0.385±0.01 within Crater S (Fig. 6C), 4% higher than the CE-6 site. The off/on ratio of LAMP data showed an average value of 1.24 ± 1 and a max value of 6 within Crater S, while the CE-7 candidate landing site was not covered by the LAMP data.

PSRs are widely distributed in the study region, mostly inside craters, and have a circular shape. Near the CE-7 candidate landing site, there are large-scale PSRs, such as PSRs within Shackleton (~232 km^2, ~15 km from the candidate site), Haynes (~86 km^2, ~24 km from the candidate landing site), and Slater (~176 km^2, ~15 km from the candidate landing site) craters. However, these PSRs are not accessible by the hopper due to high slopes and long distances (Li et al., 2025). Along the Shackleton-Slater Ridge, there are several PSRs around 1-6 km^2. Among them, Crater S hosts a PSR about 5 km^2 located ~6 km away from the CE-7 candidate site in the southeastern direction (Figs. 6B, and 7A) and is preferred to be explored by the CE-7 hopper. According to Diviner thermal measurements, the average temperature of Crater S throughout a year is ~52 K, below the surface stable temperature of CO_2 (62 K) and H_2O (110 K) (Williams et al., 2019) (Fig. S4). The CE-7 rover might also investigate several small-sized PSRs located between the candidate CE-7 landing site and Crater S, some of which are expected to have trapped and accumulated volatiles (Wueller et al., 2026a).

The ISD data suggests shallow ISD near PSRs, including Crater S and Shackleton, at a range of 0-0.5 m (Fig. 7B). At the CE-7 candidate site with solar illumination, the ice stability depth is around 2 m. At the CE-7 candidate site, the IFI was nearly zero (Fig. 7C), indicating there might not be any water ice. However, Crater S has an IFI of ~0.31, even higher than Shackleton crater (~0.16), showing Crater S is a better candidate for water ice deposits than the larger Shackleton crater.

4. Discussion

4.1. Lateral and vertical distribution of materials at the CE-7 candidate region

Laterally, whether CE-7 will land on the ejecta blanket of Shackleton crater will predominantly control the scientific outcome of the mission. In the south circumpolar geological map of Krasilnikov et al. (2023), the

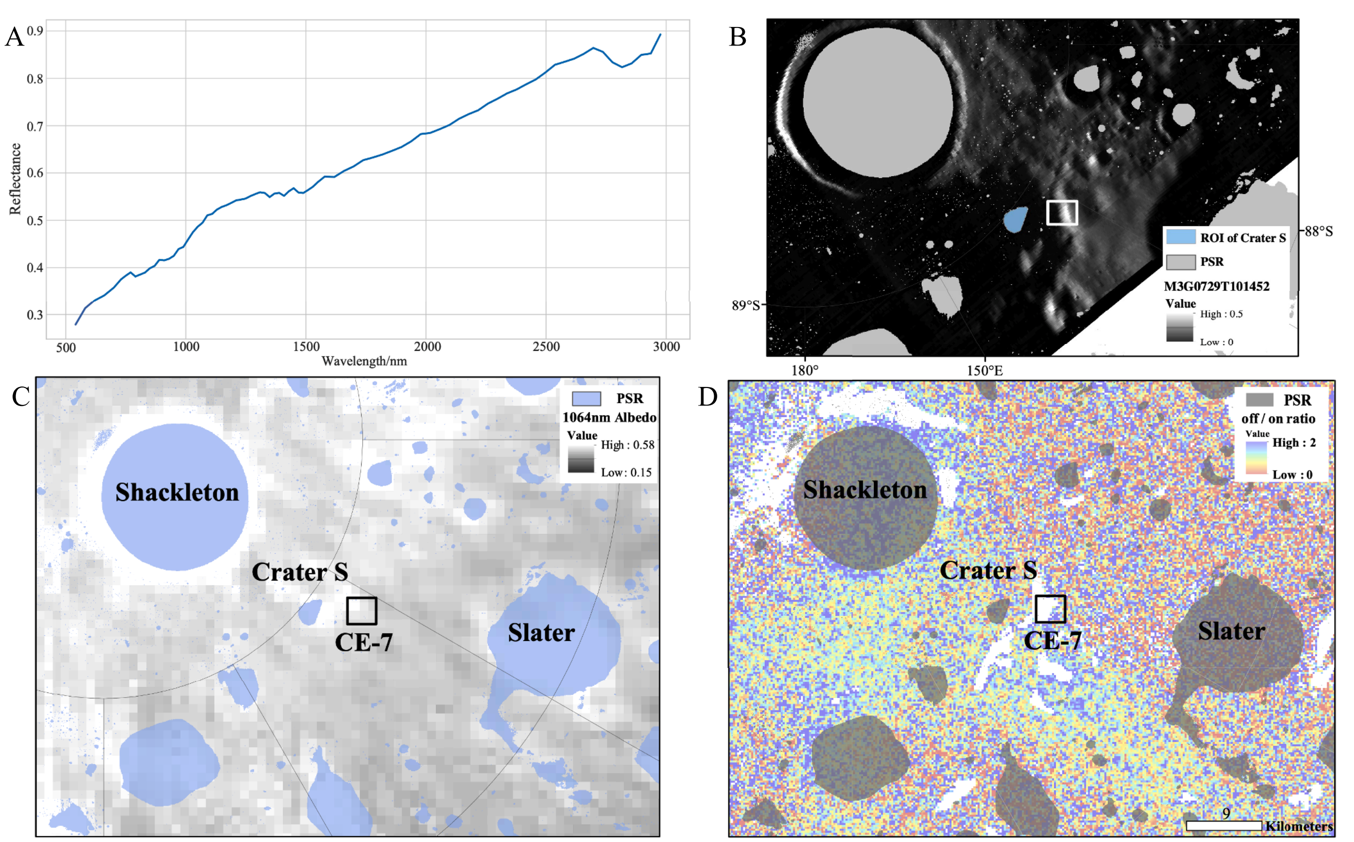

Fig. 6. (A) M^3 spectrum at CE-7 candidate site. A clear adsorption feature can be seen near 2850 nm. (B) PSR of Crater S (in blue) and M^3 data coverage of the study region; the CE-7 candidate landing site is shown in the white frame. (C) The LOLA 1064 nm reflectance data. The CE-7 candidate landing site is shown in the black frame. (D) The LAMP off/on ratio data near the CE-7 candidate landing site.

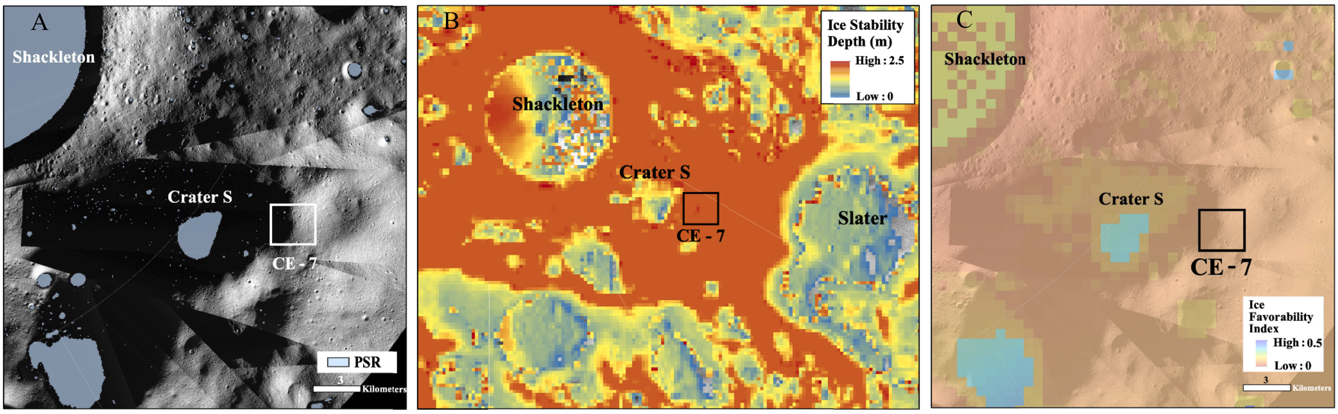

Fig. 7. (A) Detailed NAC image and PSRs of the CE-7 candidate landing region (shown in white or black frames). (B) Ice stability depth near the CE-7 candidate landing region. (C) Ice favorability index near the CE-7 candidate landing region.

ejecta blanket of Shackleton extends to ~20 km outside the crater rim, including the CE-7 candidate site. The USGS geological map (Fortezzo et al., 2020), on the other hand, identified a smaller Shackleton ejecta blanket, only 4-9 km outside the crater rim, putting the CE-7 site in a much older Pre-Nectarian-aged region. Detailed ejecta extent was mapped and calculated in (Wueller et al., 2026b), who suggest a maximum of 31 km from the crater center. Continuous ejecta usually expands 1-2 radii beyond the crater rim (Osinski et al., 2011), and the CE-7 candidate site is located at 1.6 radii beyond the crater rim, making it possible that CE-7 lies directly on its continuous ejecta. In addition, we found that the composition of the CE-7 candidate landing site and adjacent materials is mostly similar to Shackleton, and the ~15.2 m ejecta (~11.6 m foreign ejecta, and ~3.6 m mixed local materials) of Shackleton is estimated to be at the CE-7 site, not very likely to be discontinuous ejecta for this large thickness (see above). Thus, we suggest that the CE-7 candidate site is located on the continuous ejecta blanket of Shackleton, and CE-7 will primarily explore its materials.

Two of the six impact basins (Table 1) are located inside SPA, i.e., Amundsen-Ganswindt (~263 m of foreign ejecta) and Schrödinger (~35 m of foreign ejecta) basins. These two basins mainly transported SPA materials to the CE-7 site. An oblique impact was suggested for Schrödinger away from the south pole (Kring et al., 2025), resulting in only minimal Schrödinger ejecta near the south pole. Mendel-Rydberg basin (~12 m of foreign ejecta) is located at the rim of SPA, which might excavate both SPA materials and Feldspathic Highland Terrane (FHT) materials. Australe North basin (~17 m of foreign ejecta) and Orientale basin (~16 m of foreign ejecta) are approximately several hundred km away from the SPA basin rim in the FHT. Therefore, highland materials could be delivered to the CE-7 site. In addition, the second-largest lunar impact basin (Neumann et al., 2015), namely the Imbrium basin (~7 m of foreign ejecta), will transport KREEP-rich materials to the CE-7 candidate site, as it is located at the Procellarum KREEP Terrane (PKT). Compared with impact basins, major source craters are located within a much smaller distance (Fig. 3); among them, 29 source craters are located within SPA, and the remaining 13 craters are in the FHT region. All of them might provide fragments with diverse compositions to the CE-7 candidate site.

Vertically, the stratigraphy of the CE-7 candidate site was constrained. Two pathways contribute to the mixing of materials at the CE-7 candidate site: (1) Vertical excavation—the Shackleton impact overturned pre-existing distal ejecta layers from the SPA, Orientale, Schrödinger, and Imbrium basins, directly incorporating them into its ejecta blanket. (2) Lateral impact gardening—later small craters (including 29 within the SPA basin) reworked the upper Shackleton ejecta layer, adding minor SPA-derived materials laterally. These pathways explain how a site dominated by Shackleton ejecta can still access ancient basin and potentially mantle-derived lithologies, providing a clear rationale for the expected compositional diversity at the CE-7 landing site.

Based on the overlapping relationships and the obtained ejecta thickness, we constructed a first-order subsurface stratigraphy of the CE-7 candidate region (Fig. 8). The top layer of the CE-7 candidate site mainly consists of ejecta from Eratosthenian- and Imbrian-aged craters (e.g., Shackleton, Wiechert J, Antoniadi). Covered by Shackleton ejecta are basin materials from Orientale (3.81 Ga), Schrödinger (3.86 Ga), Imbrium (3.87 Ga), Mendel-Rydberg (4.13 Ga), Amundsen-Ganswindt (4.26 Ga) (Orgel et al., 2018), and Australe North (Neumann et al., 2015). We used the Maxwell Z model (Maxwell, 1977) to trace the depth of materials excavated and delivered by Shackleton crater to the CE-7 candidate site (Fig. S5). Maxwell Z model results suggested that the excavation depth might reach ~2 km, which was deep enough to re-excavate the Imbrium, Schrödinger, and Orientale basin materials (Fig. S5). If the Shackleton-Slater ridge is related to SPA, it should be older than the younger basins and may have influenced their ejecta deposition in this region, leading to different ejecta thicknesses and mixing with local materials (Wueller et al., 2026c). It could also have excavated materials from the crustal ridge itself, as evidenced by the anorthositic composition of Shackleton ejecta.

All in all, CE-7 will likely investigate materials from these three basins, together with SPA materials from lateral and vertical transport. If SPA materials were investigated, it would help to analyze the compositional heterogeneity of SPA together with previous CE-4/6 missions at other parts of the SPA basin. The SPA basin is characterized by distinct compositional zones with Ca- and Fe-rich pyroxene (SPA Compositional Anomaly), Mg-rich pyroxene (Mg-Pyroxene Annulus), and mixed pyroxenes (Heterogeneous Annulus) from the center to the exterior (Moriarty and Pieters, 2018). They might represent the distinct compositions of the crust prior to SPA impact, or SPA melt sheet differentiation (Hurwitz and Kring, 2014). Schrödinger basin materials from SPA are very likely excavated by Shackleton crater to the CE-7 candidate site (and from other craters/basins, see above). Orbital hyperspectral observations found abundant olivine outcrops on its floor (Kramer et al., 2013) and peak rings (Yamamoto et al., 2012), indicating possible mantle exposures. It will be extremely valuable to identify potential olivine-rich lithologies at the CE-7 candidate site, which likely comes from the Schrödinger basin. Furthermore, it is possible to identify SPA materials, including deep crust or even upper mantle materials in a region abundant in them (Moriarty et al., 2021), especially if a southward SPA impact is considered (Andrews-Hanna et al., 2025). These SPA materials might be OLV-rich (mantle materials), OPX-rich (deep crust or differentiation), CPX-rich (SPA Compositional Anomaly), and could be compared with those SPA materials explored by CE-4 (Huang et al., 2020) and CE-6 missions (Su et al., 2025). Altogether, they will help to piece a complex picture of the SPA

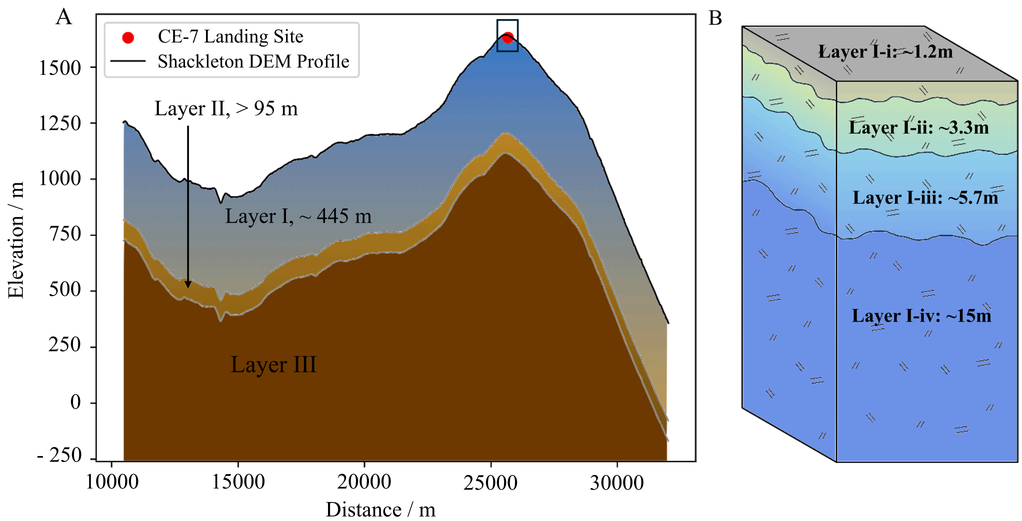

Fig. 8. (A) Vertical profile under the CE-7 candidate site. Layer I (blue): ~445 m, ejecta from Imbrian-aged basins (Orientale, Schrödinger and Imbrium); Layer II (brown):> 95 m, ejecta of Mendel-Rydberg; Layer III (dark brown): ejecta from Pre-Nectarian-aged basins (e.g. Amundsen-Ganswindt). (B) Zoom in on the black-framed region (the top layer) in (A). Layer I-i (grey): ~1.2 m, ejected material from small young craters; Layer I-ii (green): ~3.3 m, ejecta from Eratosthenian-aged craters; Layer I-iii (blue): ~5.7 m, ejecta from Imbrian-aged craters; Layer I-iv (dark blue): ~15 m, Shackleton crater ejecta.

impact, probing into the lunar interior, and providing additional constraints on SPA basin processes (Jolliff et al., 2021) and the magma ocean model (Elkins-Tanton et al., 2011). The stratigraphy of these materials could be constructed by the LPR (100 MHz-1,500 MHz, 10 MHz-110 MHz) onboard the rover; their mineralogy and composition could be measured by the LRS (300-6,000 cm^{-1}) onboard the rover together with the Lunar Neutron Gamma Spectrometer and the WISMIA onboard the orbiter.

4.2. *Volatile distribution at the CE-7 candidate landing region*

Multi-source datasets were used to analyze the volatile potentials and their characteristics at the CE-7 candidate region. As for the candidate site (Fig. 7A), M^3 spectra showed a relatively distinct water/hydroxyl absorption feature near 2.85 μm (Fig. 6). The PSR within Crater S (Fig. 7A) has an average albedo of 0.385 at 1064 nm and a maximum temperature of ~ 78 K (Williams et al., 2017). Previous analysis of LOLA 1064 nm reflectance data showed that the high albedo at low-temperature (maximum temperature < 110 K) regions could be related to the presence of potential surface water ice (Fisher et al., 2017). This agrees with the result of Crater S. As for the LAMP data, the off/on ratio would rise with water ice concentration (Hayne et al., 2015). Inside Crater S, the average ratio was ~1.24. Compared to the typical ratio of ~0.8 in regions that are not likely to possess water/ice, this indicates potential water ice inside Crater S. We note that the value of LOLA 1064 nm albedo might be related to soil maturity (Lucey et al., 2014), but the LAMP ratio should not correlate with maturity. The content of water ice, however, might be low, as the ratio was much higher (~1.73) within the PSR of Shackleton crater.

Orbital and in situ measurements of lunar south pole will provide constraints of volatiles in different scales and support each other. The detection results from the CE-7 measurements, combined with thermal stability models and capture/retention models, can facilitate a comprehensive assessment of lunar volatiles. Multiple CE-7 payloads would be able to measure low-abundance surface water, including WISMIA on orbit and IsMSV from surface. Covering a wide wavelength range from 0.45 to 10 μm (including the most obvious water absorption feature near 6 μm), WISMIA on the orbiter will be used for large-scale surface water/ice detection, including the CE-7 site and Crater S, even globally to compare with M^3 observations (Li and Milliken, 2017). IsMSV on the rover is designed specially to detect various kinds of volatiles (He, CO, Ar, etc.) on surface. These two payloads will contribute to the in situ and orbital water detection at the CE-7 site, as well as along the route of the rover that likely passes by a few PSRs. They will compare the water content/volatile types between small/big PSRs, in different thermal and geological conditions. Both WISMIA and IsMSV are more likely to capture the weak signals of potential surface water/ice than previous datasets with their wider wavelength coverage (0.45-10 μm) and sensitivity (volatile content detection limit >0.01 wt.%) (Wang et al., 2024), respectively.

In addition, LSWMA will be onboard the CE-7 hopper. It will investigate Crater S for its surface/subsurface water contents and hydrogen/oxygen isotopes concurrently (Chen et al., 2024). Lunar soils will be collected and heated to extract any potential water ice, and loaded into the measurement mechanism to be analyzed by the miniaturized tunable laser spectrometer (Li et al., 2025). The current three major sources of lunar water include solar wind, volcanic activities, and asteroid impacts (also cometary impacts and micrometeoroid bombardment) (Anand et al., 2014; Head et al., 2020; Zhou et al., 2024). Measuring hydrogen isotopes could enable interpretation of their potential sources. Any surface volatiles in Crater S were likely removed or buried by the Shackleton impact (Wueller et al., 2026c). Thus, the potentially exist volatile must have been subsequently delivered or migrated.

Even if there is no surface water identified, the hopper could drill down up to 1 m to extract subsurface soils, at which depth water ice should be stable and may exist. In addition, the LPR that is expected to detect subsurface structures deeper than 40 m (for 100 MHz–1,500 MHz) or even 400 m (for 10 MHz–110 MHz). The subsurface water ice could be detected because its physical properties differ from lunar soils, especially its dielectric constant controlling the propagation of radar echoes (ice: $\varepsilon = 3$; lunar soil: $\varepsilon = 5$) (Zhao et al., 2025). As discussed above, even at the CE-7 candidate site, large-scale surface water ice exposures are unlikely to exist, but are predicted to be stable at a depth of >2 m, fully in the region of discernibility by LPR.

5. Conclusions

In this study, we established a comprehensive geological context for the CE-7 candidate site at Shackleton-Slater Ridge to support this upcoming south pole mission. Our key findings are summarized below:

1. Geological Setting and Material Provenance: The candidate landing site is located on Shackleton crater's continuous ejecta blanket, approximately 1.6 crater radii from the rim. Provenance analysis indicates that Shackleton crater is the predominant source of local

materials, contributing ~11.6 m of primary ejecta. In addition, 29 key source craters from within the SPA basin contribute to the local regolith, delivering a mixed assemblage of SPA-related lithologies. Materials from impact basins, including the Amundsen-Ganswindt, Schrödinger, and Orientale basins, were calculated to be buried at several hundred meters depths. Excavation by the Shackleton impact could have exposed these deeper SPA and other basins' materials on the surface, making them accessible for CE-7 payloads.
2. Compositional Characteristics: The surface materials at the landing site are compositionally uniform, dominated by anorthosite (~80% plagioclase) with a low-Ca pyroxene (LCP) component (~10%). This lithology is consistent with the magnesium-rich, noritic composition expected for materials within the SPA basin's influence. High-Ca pyroxene (HCP) and TiO_2 are notably low in the CE-7 candidate landing region, further supporting a non-mare, feldspathic-rich provenance.
3. Volatile Assessment: Multi-dataset analysis of the PSR within Crater S and the CE-7 candidate landing region reveals evidence for the possible existence of surface water/ice. M^3 spectra show an absorption feature of hydroxyl, and LOLA reflectance data show high reflectance inside the PSR. Subsurface ice could exist ~2 m under the candidate landing site. The CE-7 mission's scientific payloads, particularly the LSWMA, are crucial for detecting these potentially elusive volatile signals.
4. Scientific Implications: The CE-7 mission aims to explore the lunar south polar region. By investigating materials associated with Shackleton, other local craters, and potentially deep basin ejecta, CE-7 will provide ground-truth data for models of SPA composition and evolution. Furthermore, its volatile search will directly test hypotheses regarding water sources and migration in permanently shadowed regions. The findings from this study offer a predictive framework for interpreting the data that CE-7 will return, bridging the gap between orbital remote sensing and in situ analysis.

CRediT authorship contribution statement

Mingyu Tian: Writing – review & editing, Writing – original draft, Visualization, Validation, Methodology, Investigation, Formal analysis, Data curation, Conceptualization. **Yuqi Qian:** Writing – review & editing, Writing – original draft, Validation, Supervision, Resources, Methodology, Investigation, Funding acquisition, Conceptualization. **Lukas Wueller:** Writing – review & editing, Validation, Methodology, Investigation. **James Head:** Writing – review & editing, Validation, Methodology, Investigation. **Xiang Li:** Writing – review & editing, Validation, Investigation. **Wajiha Iqbal:** Writing – review & editing, Validation, Investigation. **Harald Hiesinger:** Writing – review & editing, Validation. **Carolyn van der Bogert:** Writing – review & editing, Validation. **Ke Xu:** Writing – review & editing, Validation. **Lingzhi Sun:** Writing – review & editing, Methodology. **Long Xiao:** Writing – review & editing, Validation. **Guochun Zhao:** Writing – review & editing, Supervision, Project administration, Funding acquisition.

Declaration of competing interest

The authors declare that they have no known competing financial interests or personal relationships that could have appeared to influence the work reported in this paper.

Acknowledgements

This research was funded by HK RGC 17307025, 17300526, 17306623, and JLFS/P-702/24. LW, WI, and CvdB are supported by German Aerospace Agency (DLR) Grant 50OW2402 for participation in the Lunar Reconnaissance Orbiter (LRO) Camera (LROC) Team.

Supplementary materials

Supplementary material associated with this article can be found, in the online version, at doi:10.1016/j.epsl.2026.120349.

Data availability

Data are accessible through the links provided in the paper.

References

Anand, M., Tartèse, R., Barnes, J.J., 2014. Understanding the origin and evolution of water in the Moon through lunar sample studies. Phil. Trans. R. Soc. A. 372, 20130254. https://doi.org/10.1098/rsta.2013.0254.

Andrews-Hanna, J.C., Bottke, W.F., Broquet, A., Evans, A.J., Gowman, G., Johnson, B.C., Keane, J.T., Levin, J.N., Mallik, A., Marchi, S., Moruzzi, S.A., Roy, A., Wakita, S., 2025. Southward impact excavated magma ocean at the lunar South Pole–Aitken basin. Nature 646, 297–302. https://doi.org/10.1038/s41586-025-09582-y.

Archinal, B., Weller, L., Richie, J., Lee, E., Bennett, K., Speyerer, E., Tyburczy, T., 2023. Controlled high-resolution LROC NAC polar mosaics. In: Presented at the 54th Lunar and Planetary Science Conference, p. 2333.

Barker, M.K., Mazarico, E., Neumann, G.A., Smith, D.E., Zuber, M.T., Head, J.W., Sun, X., 2023. A new view of the lunar south pole from the lunar orbiter laser altimeter (LOLA). Planet. Sci. J. 4, 183. https://doi.org/10.3847/PSJ/acf3e1.

Bernhardt, H., Walsh, J.M., Schröder, L.M., Clark, J.D., Henriksen, M.R., Edwards, C.S., 2025. Numeric ring-reconstructions based on massifs favor a non-oblique south pole-Aitken-forming impact event. Earth Planet. Sci. Lett. 650, 119123. https://doi.org/10.1016/j.epsl.2024.119123.

Boazman, Sarah.J., Shah, J., Harish, Gawronska, A.J., Halim, S.H., Satyakumar, A.V., Gilmour, C.M., Bickel, V.T., Barrett, N., Kring, D.A., 2022. The distribution and accessibility of geologic targets near the lunar south pole and candidate artemis landing sites. Planet. Sci. J. 3, 275. https://doi.org/10.3847/PSJ/aca590.

Cannon, K.M., Britt, D.T., 2020. A geologic model for lunar ice deposits at mining scales. Icarus 347, 113778. https://doi.org/10.1016/j.icarus.2020.113778.

Chen, R., Lu, W., Li, X., Wang, X., Chen, K., Zhang, C., Cao, N., Xu, Z., Xu, Y., Kan, R., Liu, R., Yang, Q., Zhang, L., 2024. Chang'E-7 lunar soil water molecule analyzer (LSWMA) prototype for high-precision measurement of water content and hydrogen isotope ratio. J. Earth Sci. 35, 2180–2182. https://doi.org/10.1007/s12583-024-2023-7.

Croft, S.K., 1985. The scaling of complex craters. J. Geophys. Res.: Solid Earth 90, C828–C842.

Deutsch, A.N., Head, J.W., Neumann, G.A., 2020. Analyzing the ages of south polar craters on the moon: implications for the sources and evolution of surface water ice. Icarus 336, 113455. https://doi.org/10.1016/j.icarus.2019.113455.

Elkins-Tanton, L.T., Burgess, S., Yin, Q.-Z., 2011. The lunar magma ocean: reconciling the solidification process with lunar petrology and geochronology. Earth Planet. Sci. Lett. 304, 326–336. https://doi.org/10.1016/j.epsl.2011.02.004.

Fisher, E.A., Lucey, P.G., Lemelin, M., Greenhagen, B.T., Siegler, M.A., Mazarico, E., Aharonson, O., Williams, J.-P., Hayne, P.O., Neumann, G.A., Paige, D.A., Smith, D. E., Zuber, M.T., 2017. Evidence for surface water ice in the lunar polar regions using reflectance measurements from the lunar orbiter laser altimeter and temperature measurements from the diviner lunar radiometer experiment. Icarus 292, 74–85. https://doi.org/10.1016/j.icarus.2017.03.023.

Flahaut, J., Carpenter, J., Williams, J.-P., Anand, M., Crawford, I.A., Van Westrenen, W., Füri, E., Xiao, L., Zhao, S., 2020. Regions of interest (ROI) for future exploration missions to the lunar south pole. Planet. Space Sci. 180, 104750. https://doi.org/10.1016/j.pss.2019.104750.

Fortezzo, C., Spudis, P., Harrel, S., 2020. Release of the digital unified global geologic map of the moon at 1: 5,000,000-scale. In: Presented at the 51st annual lunar and planetary science conference, p. 2760.

Frueh, T., Camon, A., Boyce, M., Halwa, S.L., Ligeza, G., Lemelin, M., Thomson, B.J., Kring, D.A., 2025. Impact resurfacing of the artemis exploration zone: sample locations for primordial crust and south pole-Aitken (SPA) ejecta. JGR Planets 130, e2025JE009050. https://doi.org/10.1029/2025JE009050.

Gawronska, A.J., Boazman, S.J., 2025. Characteristics of the Shackleton-de Gerlache ridge and implications for lunar south polar geology and future sampling activities. Icarus 441, 116719. https://doi.org/10.1016/j.icarus.2025.116719.

Gladstone, G.R., Retherford, K.D., Egan, A.F., Kaufmann, D.E., Miles, P.F., Parker, J.W., Horvath, D., Rojas, P.M., Versteeg, M.H., Davis, M.W., Greathouse, T.K., Slater, D.C., Mukherjee, J., Steffl, A.J., Feldman, P.D., Hurley, D.M., Pryor, W.R., Hendrix, A.R., Mazarico, E., Stern, S.A., 2012. Far-ultraviolet reflectance properties of the moon's permanently shadowed regions. J. Geophys. Res. 117, 2011JE003913. https://doi.org/10.1029/2011JE003913.

Green, R.O., Pieters, C., Mouroulis, P., Eastwood, M., Boardman, J., Glavich, T., Isaacson, P., Annadurai, M., Besse, S., Barr, D., Buratti, B., Cate, D., Chatterjee, A., Clark, R., Cheek, L., Combe, J., Dhingra, D., Essandoh, V., Geier, S., Goswami, J.N., Green, R., Haemmerle, V., Head, J., Hovland, L., Hyman, S., Klima, R., Koch, T., Kramer, G., Kumar, A.S.K., Lee, K., Lundeen, S., Malaret, E., McCord, T., McLaughlin, S., Mustard, J., Nettles, J., Petro, N., Plourde, K., Racho, C., Rodriquez, J., Runyon, C., Sellar, G., Smith, C., Sobel, H., Staid, M., Sunshine, J., Taylor, L., Thaisen, K., Tompkins, S., Tseng, H., Vane, G., Varanasi, P., White, M., Wilson, D., 2011. The moon mineralogy mapper (M^3) imaging spectrometer for lunar science: instrument description, calibration, on-orbit measurements, science data

calibration and on-orbit validation. J. Geophys. Res. 116, E00G19. https://doi.org/10.1029/2011JE003797.
Haruyama, J., Matsunaga, T., Ohtake, M., Morota, T., Honda, C., Yokota, Y., Torii, M., Ogawa, Y., LISM Working Group, 2008. Global lunar-surface mapping experiment using the lunar imager/spectrometer on SELENE. Earth Planet Sp. 60, 243–255. https://doi.org/10.1186/BF03352788.
Hawke, B.R., Blewett, D.T., Lucey, P.G., Smith, G.A., Bell, J.F., Campbell, B.A., Robinson, M.S., 2004. The origin of lunar crater rays. Icarus 170, 1–16. https://doi.org/10.1016/j.icarus.2004.02.013.
Hayne, P.O., Hendrix, A., Sefton-Nash, E., Siegler, M.A., Lucey, P.G., Retherford, K.D., Williams, J.-P., Greenhagen, B.T., Paige, D.A., 2015. Evidence for exposed water ice in the MOON'S south polar regions from lunar reconnaissance orbiter ultraviolet albedo and temperature measurements. Icarus 255, 58–69. https://doi.org/10.1016/j.icarus.2015.03.032.
Head, J.W., Wilson, L., Deutsch, A.N., Rutherford, M.J., Saal, A.E., 2020. Volcanically induced transient atmospheres on the moon: assessment of duration, significance, and contributions to polar volatile traps. Geophys. Res. Lett. 47, e2020GL089509. https://doi.org/10.1029/2020GL089509.
Huang (黄俊), J., Xiao (肖智勇), Z., Xiao (肖龙), L., Horgan, B., Hu (胡晓依), X., Lucey, P., Xiao (肖潇), X., Zhao (赵思源), S., Qian (钱煜奇), Y., Zhang (张昊), H., Li (李春来), C., Xu (徐睿), R., He (何志平), Z., Yang (杨建峰), J., Xue (薛彬), B., He (何琦), Q., Zhong (钟杰), J., Lin (林宏宇), H., Huang (黄长宁), C., Xie (谢剑锋), J., 2020. Diverse rock types detected in the lunar south pole–Aitken basin by the Chang'E-4 lunar mission. Geology 48, 723–727. https://doi.org/10.1130/G47280.1.
Hurwitz, D.M., Kring, D.A., 2014. Differentiation of the south pole–Aitken basin impact melt sheet: implications for lunar exploration. JGR Planets 119, 1110–1133. https://doi.org/10.1002/2013JE004530.
Iqbal, W., Wueller, L., Poehler, C.M., Van Der Bogert, C.H., Hiesinger, H., Ivanov, M.A., Wright, J., Head, J.W., Oetting, A., Jolliff, B.L., 2026. Geological mapping of the south pole-Aitken (SPA) basin region of the moon. Icarus 459, 117234. https://doi.org/10.1016/j.icarus.2026.117234.
Jolliff, B., Petro, N., Moriarty, D., Ryan Watkins, P., Head III, J., Potter, R., 2021. Sample return from the moon's south pole-Aitken Basin. Bull. Am. Astron. Soc. 53, 290.
Klima, R.L., Pieters, C.M., Dyar, M.D., 2007. Spectroscopy of synthetic Mg-Fe pyroxenes I: spin-allowed and spin-forbidden crystal field bands in the visible and near-infrared. Meteorit. Planet. Scien. 42, 235–253. https://doi.org/10.1111/j.1945-5100.2007.tb00230.x.
Kramer, G.Y., Kring, D.A., Nahm, A.L., Pieters, C.M., 2013. Spectral and photogeologic mapping of schrödinger basin and implications for post-south pole-Aitken impact deep subsurface stratigraphy. Icarus 223, 131–148. https://doi.org/10.1016/j.icarus.2012.11.008.
Krasilnikov, S.S., Ivanov, M.A., Head, J.W., Krasilnikov, A.S., 2023. Geologic history of the south circumpolar region (SCR) of the moon. Icarus 394, 115422. https://doi.org/10.1016/j.icarus.2022.115422.
Kring, D.A., Kramer, G.Y., Bussey, D.B.J., Hurley, D.M., Stickle, A.M., Van Der Bogert, C.H., 2021. Prominent volcanic source of volatiles in the south polar region of the moon. Adv. Space Res. 68, 4691–4701. https://doi.org/10.1016/j.asr.2021.09.008.
Kring, D.A., Kallenborn, D.P., Collins, G.S., 2025. Grand canyons on the moon. Nat. Commun. 16, 1146. https://doi.org/10.1038/s41467-024-55675-z.
Lemelin, M., Lucey, P.G., Camon, A., 2022. Compositional maps of the lunar polar regions derived from the kaguya spectral profiler and the lunar orbiter laser altimeter data. Planet. Sci. J. 3, 63. https://doi.org/10.3847/PSJ/ac532c.
Li, S., Milliken, R.E., 2017. Water on the surface of the moon as seen by the moon mineralogy mapper: distribution, abundance, and origins. Sci. Adv. 3, e1701471. https://doi.org/10.1126/sciadv.1701471.
Li, S., Lucey, P.G., Milliken, R.E., Hayne, P.O., Fisher, E., Williams, J.-P., Hurley, D.M., Elphic, R.C., 2018. Direct evidence of surface exposed water ice in the lunar polar regions. Proc. Natl. Acad. Sci. USA 115, 8907–8912. https://doi.org/10.1073/pnas.1802345115.
Li, X., Cao, N., Kan, R., Xu, Z., Zhang, X., Wang, Q., Lu, W., Chen, R., Wang, X., Deng, H., Li, R., 2025. Miniaturized tunable laser spectrometer for the simultaneous detection of water ice and hydrogen–oxygen isotopes for the Chang'E-7 lunar soil water molecule analyzer. ACS Sens. 10, 4679–4686. https://doi.org/10.1021/acssensors.5c01115.
Lucey, P.G., Neumann, G.A., Riner, M.A., Mazarico, E., Smith, D.E., Zuber, M.T., Paige, D.A., Bussey, D.B., Cahill, J.T., McGovern, A., Isaacson, P., Corley, L.M., Torrence, M.H., Melosh, H.J., Head, J.W., Song, E., 2014. The global albedo of the moon at 1064 nm from LOLA: the global albedo of the moon from LOLA. J. Geophys. Res. Planets 119, 1665–1679. https://doi.org/10.1002/2013JE004592.
Maxwell, D.E., 1977. Simple Z model for cratering, ejection, and the overturned flap. In: Presented at the Impact and explosion cratering: Planetary and terrestrial implications, pp. 1003–1008.
Mazarico, E., Neumann, G.A., Smith, D.E., Zuber, M.T., Torrence, M.H., 2011. Illumination conditions of the lunar polar regions using LOLA topography. Icarus 211, 1066–1081. https://doi.org/10.1016/j.icarus.2010.10.030.
Melosh, H.J., Kendall, J., Horgan, B., Johnson, B.C., Bowling, T., Lucey, P.G., Taylor, G.J., 2017. South Pole–Aitken basin ejecta reveal the Moon's upper mantle. Geology 45 (12), 1063–1066. https://doi.org/10.1130/g39375.1. (Accessed 3 October 2017).
Miljković, K., Wieczorek, M.A., Collins, G.S., Laneuville, M., Neumann, G.A., Melosh, H.J., Solomon, S.C., Phillips, R.J., Smith, D.E., Zuber, M.T., 2013. Asymmetric distribution of lunar impact basins caused by variations in target properties. Science 342, 724–726. https://doi.org/10.1126/science.1243224.
Moriarty, D.P., Petro, N.E., 2024. Mineralogical characterization of the lunar south polar region: 1. The artemis exploration zone. JGR Planets 129, e2023JE008266. https://doi.org/10.1029/2023JE008266.
Moriarty, D.P., Pieters, C.M., 2018. The character of south pole-Aitken basin: patterns of surface and subsurface composition. JGR Planets 123, 729–747. https://doi.org/10.1002/2017JE005364.
Moriarty, D.P., Watkins, R.N., Valencia, S.N., Kendall, J.D., Evans, A.J., Dygert, N., Petro, N.E., 2021. Evidence for a Stratified Upper Mantle Preserved Within the South Pole-Aitken Basin. J. Geophys. Res. Planets 126 (1), e2020JE006589. https://doi.org/10.1029/2020je006589. (Accessed 26 January 2021).
Neumann, G.A., Zuber, M.T., Wieczorek, M.A., Head, J.W., Baker, D.M.H., Solomon, S.C., Smith, D.E., Lemoine, F.G., Mazarico, E., Sabaka, T.J., Goossens, S.J., Melosh, H.J., Phillips, R.J., Asmar, S.W., Konopliv, A.S., Williams, J.G., Sori, M.M., Soderblom, J.M., Miljković, K., Andrews-Hanna, J.C., Nimmo, F., Kiefer, W.S., 2015. Lunar impact basins revealed by gravity recovery and interior laboratory measurements. Sci. Adv. 1, e1500852. https://doi.org/10.1126/sciadv.1500852.
Oberbeck, V., Hörz, F., Morrison, R., Quaide, W., Gault, D., 1975. On the origin of the lunar smooth-plains. Moon 12, 19–54.
Orgel, C., Michael, G., Fassett, C.I., van der Bogert, C.H., Riedel, C., Kneissl, T., Hiesinger, H., 2018. Ancient bombardment of the inner solar system: reinvestigation of the “fingerprints” of different impactor populations on the lunar surface. JGR Planets 123, 748–762. https://doi.org/10.1002/2017JE005451.
Osinski, G.R., Tornabene, L.L., Grieve, R.A.F., 2011. Impact ejecta emplacement on terrestrial planets. Earth Planet. Sci. Lett. 310 (3-4), 167–181. https://doi.org/10.1016/j.epsl.2011.08.012.
Pieters, C.M., Goswami, J.N., Clark, R.N., Annadurai, M., Boardman, J., Buratti, B., Combe, J.-P., Dyar, M.D., Green, R., Head, J.W., Hibbitts, C., Hicks, M., Isaacson, P., Klima, R., Kramer, G., Kumar, S., Livo, E., Lundeen, S., Malaret, E., McCord, T., Mustard, J., Nettles, J., Petro, N., Runyon, C., Staid, M., Sunshine, J., Taylor, L.A., Tompkins, S., Varanasi, P., 2009. Character and spatial distribution of OH/H_2 O on the surface of the moon seen by M^3 on Chandrayaan-1. Science 326, 568–572. https://doi.org/10.1126/science.1178658.
Qiao, L., Xu, L., Head, J.W., Chen, J., Zhang, Y., Li, B., Ling, Z., 2024. Geological evidence for extensive basin ejecta as plains terrains in the moon's south polar region. Nat. Commun. 15, 5783. https://doi.org/10.1038/s41467-024-50155-w.
Qiu, D., Chen, W., Yan, J., Yi, S., 2025. FeO and TiO_2 maps of the lunar polar regions derived from the clementine data. JGR Planets 130, e2024JE008753. https://doi.org/10.1029/2024JE008753.
Sharpton, V.L., 2014. Outcrops on lunar crater rims: implications for rim construction mechanisms, ejecta volumes and excavation depths. JGR Planets 119, 154–168. https://doi.org/10.1002/2013JE004523.
Siegler, M.A., Miller, R.S., Keane, J.T., Laneuville, M., Paige, D.A., Matsuyama, I., Lawrence, D.J., Crotts, A., Poston, M.J., 2016. Lunar true polar wander inferred from polar hydrogen. Nature 531, 480–484. https://doi.org/10.1038/nature17166.
Spudis, P.D., Bussey, B., Plescia, J., Josset, J., Beauvivre, S., 2008. Geology of shackleton crater and the south pole of the moon. Geophys. Res. Lett. 35, 2008GL034468. https://doi.org/10.1029/2008GL034468.
Sruthi, U., Senthil Kumar, P., 2014. Volcanism on farside of the moon: new evidence from antoniadi in south pole Aitken basin. Icarus 242, 249–268. https://doi.org/10.1016/j.icarus.2014.07.030.
Stöffler, D., Knöll, H.-D., Marvin, U., Simonds, C., Warren, P.H., 1980. Recommended classification and nomenclature of lunar highland rocks-a committee report. In: Presented at the Lunar highlands crust, pp. 51–70.
Su, B., Chen, Y., Wang, Z., Zhang, D., Chen, H., Gou, S., Yue, Z., Liu, Y., Yuan, J., Tang, G., Guo, S., Li, Q., Lin, Y.-T., Li, X.-H., Wu, F.-Y., 2025. South pole–Aitken massive impact 4.25 billion years ago revealed by Chang'e-6 samples. Natl. Sci. Rev. 12, nwaf103. https://doi.org/10.1093/nsr/nwaf103.
Tye, A.R., Fassett, C.I., Head, J.W., Mazarico, E., Basilevsky, A.T., Neumann, G.A., Smith, D.E., Zuber, M.T., 2015. The age of lunar south circumpolar craters Haworth, Shoemaker, Faustini, and Shackleton: implications for regional geology, surface processes, and volatile sequestration. Icarus 255, 70–77. https://doi.org/10.1016/j.icarus.2015.03.016.
Wagner, R., Speyerer, E., Robinson, M., LROC team, 2015. New mosaicked data products from the LROC team. In: Presented at the 46th annual lunar and planetary science conference, p. 1473.
Wang, Y., Wu, B., Xue, H., Li, X., Ma, J., 2021. An improved global catalog of lunar impact craters (≥1 km) with 3D morphometric information and updates on global crater analysis. JGR Planets 126, e2020JE006728. https://doi.org/10.1029/2020JE006728.
Wang, C., Jia, Y., Xue, C., Lin, Y., Liu, J., Fu, X., Xu, L., Huang, Y., Zhao, Y., Xu, Y., Gao, R., Wei, Y., Tang, Y., Yu, D., Zou, Y., 2024. Scientific objectives and payload configuration of the Chang'E-7 mission. Natl. Sci. Rev. 11, nwad329. https://doi.org/10.1093/nsr/nwad329.
Williams, J.-P., Paige, D.A., Greenhagen, B.T., Sefton-Nash, E., 2017. The global surface temperatures of the moon as measured by the diviner lunar radiometer experiment. Icarus 283, 300–325. https://doi.org/10.1016/j.icarus.2016.08.012.
Williams, J.-P., Greenhagen, B.T., Paige, D.A., Schorghofer, N., Sefton-Nash, E., Hayne, P.O., Lucey, P.G., Siegler, M.A., Aye, K.M., 2019. Seasonal polar temperatures on the moon. JGR Planets 124, 2505–2521. https://doi.org/10.1029/2019JE006028.
Wueller, L., Iqbal, W., Frueh, T., Van Der Bogert, C.H., Hiesinger, H., 2024. Geologic history of the amundsen crater region near the lunar south pole: basis for future exploration. Planet. Sci. J. 5, 147. https://doi.org/10.3847/PSJ/ad2c04.
Wueller, L., Iqbal, W., Frueh, T., Head, J.W., Kring, D.A., Oetting, A., Van Der Bogert, C.H., Hiesinger, H., 2025. Geologic history of the mons malapert and mons mouton regions near the lunar south pole: basis for future exploration. JGR Planets 130, e2025JE009127. https://doi.org/10.1029/2025JE009127.
Wueller, L., Berger, L.M., Christopher, H., Sugimoto, K., Thaker, A.D., Carton, L., Jo, W., Lee, S., Pedrelli, R., Sanchez, P., Kring, D.A., 2026a. Assessing potential landing sites

with favorable illumination and accessible, potentially volatile-rich permanently shadowed regions within artemis candidate landing regions. JGR Planets 131, e2025JE009434. https://doi.org/10.1029/2025JE009434.

Wueller, L., Qian, Y., Frueh, T., Head III, J., Iqbal, W., Tian, M., Gao, A., Van Der Bogert, C.H., Hiesinger, H., 2026b. Geologic history of the shackleton crater region near the lunar south pole: basis for future exploration and science activities. Planet. Sci. J. Submitted.

Wueller, L., Qian, Y., Frueh, T., Head, J.W., Iqbal, W., Tian, M., Gao, A., Van Der Bogert, C.H., Hiesinger, H., 2026c. Geologic history of the shackleton crater region near the lunar south pole: basis for future exploration and science activities. Planet. Sci. J. 7, 174. https://doi.org/10.3847/PSJ/ae8258.

Xie, M., Zhu, M.-H., 2016. Estimates of primary ejecta and local material for the orientale basin: implications for the formation and ballistic sedimentation of multi-ring basins. Earth Planet. Sci. Lett. 440, 71–80. https://doi.org/10.1016/j.epsl.2016.02.012.

Xu, L., Xie, M., 2020. Ejecta thickness distribution of the Schrödinger basin on the moon. JGR Planets 125, e2020JE006506. https://doi.org/10.1029/2020JE006506.

Xu, L., Zhang, X., Qiao, L., Lai, J., 2021. Evaluating the thickness and stratigraphy of ejecta materials at the Chang'e-4 landing site. AJ 162, 29. https://doi.org/10.3847/1538-3881/abf8b0.

Yamamoto, S., Nakamura, R., Matsunaga, T., Ogawa, Y., Ishihara, Y., Morota, T., Hirata, N., Ohtake, M., Hiroi, T., Yokota, Y., Haruyama, J., 2012. Olivine-rich exposures in the South Pole-Aitken Basin. Icarus 218 (1), 331–344. https://doi.org/10.1016/j.icarus.2011.12.012.

Yamamoto, S., Matsunaga, T., Ogawa, Y., Nakamura, R., Yokota, Y., Ohtake, M., Haruyama, J., Morota, T., Honda, C., Hiroi, T., Kodama, S., 2014. Calibration of NIR 2 of spectral profiler onboard kaguya/SELENE. IEEE Trans. Geosci. Remote Sens. 52, 6882–6898. https://doi.org/10.1109/TGRS.2014.2304581.

Zhao, C., Zhang, L., Lu, S., Gao, R., 2025. Research and prospect of ground-penetrating radar on the moon. J. Geophys. Eng. 22, 1431–1447. https://doi.org/10.1093/jge/gxaf084.

Zhou, C., Mo, B., Tang, H., Gu, Y., Li, X., Zhu, D., Yu, W., Liu, J., 2024. Multiple sources of water preserved in impact glasses from Chang'e-5 lunar soil. Sci. Adv. 10, eadl2413. https://doi.org/10.1126/sciadv.adl2413.